



Big Three Dragons: Molecular Gas in a Bright Lyman-break Galaxy at $z = 7.15$

Downloaded from: <https://research.chalmers.se>, 2024-03-20 11:31 UTC

Citation for the original published paper (version of record):

Hashimoto, T., Inoue, A., Sugahara, Y. et al (2023). Big Three Dragons: Molecular Gas in a Bright Lyman-break Galaxy at $z = 7.15$. *Astrophysical Journal*, 952(1).
<http://dx.doi.org/10.3847/1538-4357/acdd5c>

N.B. When citing this work, cite the original published paper.



Big Three Dragons: Molecular Gas in a Bright Lyman-break Galaxy at $z = 7.15$

Takuya Hashimoto¹, Akio K. Inoue^{2,3}, Yuma Sugahara^{3,4}, Yoshinobu Fudamoto^{3,4}, Seiji Fujimoto^{5,6,15}, K. K. Knudsen⁷, Hiroshi Matsuo^{4,8}, Yoichi Tamura⁹, Satoshi Yamanaka¹⁰, Yuichi Harikane^{11,12}, Nario Kuno¹, Yoshiaki Ono¹¹, Dragan Salak^{13,14}, and Nozomi Ishii¹

¹ Tomonaga Center for the History of the Universe (TCHoU), Faculty of Pure and Applied Sciences, University of Tsukuba, Tsukuba, Ibaraki 305-8571, Japan; hashimoto.takuya.ga@u.tsukuba.ac.jp

² Department of Physics, School of Advanced Science and Engineering, Waseda University, 3-4-1, Okubo, Shinjuku, Tokyo 169-8555, Japan

³ Waseda Research Institute for Science and Engineering, Faculty of Science and Engineering, Waseda University, 3-4-1, Okubo, Shinjuku, Tokyo 169-8555, Japan

⁴ National Astronomical Observatory of Japan, 2-21-1 Osawa, Mitaka, Tokyo 181-8588, Japan

⁵ Cosmic Dawn Center (DAWN), Copenhagen, Denmark

⁶ Niels Bohr Institute, University of Copenhagen, Jagtvej 128, DK-2200 Copenhagen N, Denmark

⁷ Department of Space, Earth and Environment, Chalmers University of Technology, Onsala Space Observatory, SE-43992 Onsala, Sweden

⁸ Graduate University for Advanced Studies (SOKENDAI), 2-21-1 Osawa, Mitaka, Tokyo 181-8588, Japan

⁹ Department of Physics, Graduate School of Science, Nagoya University, Nagoya 464-8602, Japan

¹⁰ General Education Department, National Institute of Technology, Toba College, 1-1, Ikegami-cho, Toba, Mie 517-8501, Japan

¹¹ Institute for Cosmic Ray Research, The University of Tokyo, 5-1-5 Kashiwanoha, Kashiwa, Chiba 277-8582, Japan

¹² Department of Physics and Astronomy, University College London, Gower Street, London WC1E 6BT, UK

¹³ Institute for the Advancement of Higher Education, Hokkaido University, Kita 17 Nishi 8, Kita-ku, Sapporo, Hokkaido 060-0817, Japan

¹⁴ Department of Cosmosciences, Graduate School of Science, Hokkaido University, Kita 10 Nishi 8, Kita-ku, Sapporo, Hokkaido 060-0810, Japan

¹⁵ Department of Astronomy, The University of Texas at Austin, Austin, TX, USA

Received 2022 March 2; revised 2023 June 8; accepted 2023 June 9; published 2023 July 18

Abstract

We report Atacama Large Millimeter/submillimeter Array Band 3 observations of CO(6–5), CO(7–6), and [C I](2–1) in B14-65666 (“Big Three Dragons”), one of the brightest Lyman-break galaxies at $z > 7$ in the rest-frame ultraviolet continuum, far-infrared continuum, and emission lines of [O III] 88 μm and [C II] 158 μm . CO(6–5), CO(7–6), and [C I](2–1), whose 3σ upper limits on the luminosities are approximately 40 times fainter than the [C II] luminosity, are all not detected. The $L_{[\text{C I}]}/L_{\text{CO}(6-5)}$ and $L_{[\text{C I}]}/L_{\text{CO}(7-6)}$ ratios are higher than the typical ratios obtained in dusty star-forming galaxies or quasar host galaxies at similar redshifts, and they may suggest a lower gas density in the photodissociated region in B14-65666. By using the (1) [C II] luminosity, (2) dust mass-to-gas mass ratio, and (3) a dynamical mass estimate, we find that the molecular gas mass (M_{mol}) is $(0.05\text{--}11) \times 10^{10} M_{\odot}$. This value is consistent with the upper limit inferred from the nondetection of mid- J CO and [C I](2–1). Despite the large uncertainty in M_{mol} , we estimate a molecular gas-to-stellar mass ratio (μ_{gas}) of 0.65–140 and a gas depletion time (τ_{dep}) of 2.5–550 Myr; these values are broadly consistent with those of other high-redshift galaxies. B14-65666 could be an ancestor of a passive galaxy at $z \gtrsim 4$ if no gas is fueled from outside the galaxy.

Unified Astronomy Thesaurus concepts: High-redshift galaxies (734); Galaxies (573); Interstellar medium (847)

1. Introduction

Understanding the properties of molecular gas through cosmic time is an important topic in galaxy formation and evolution, as molecular gas is the fuel for star formation. The molecular gas mass, M_{mol} , is often determined from the luminosity of carbon monoxide ($^{12}\text{C}^{16}\text{O}$, hereafter written as simply “CO”; e.g., Bolatto et al. 2013), dust mass (e.g., Magdis et al. 2012), and radiation from cold dust sensitive to dust mass (e.g., Scoville et al. 2016). Based on M_{mol} estimates, previous studies have shown that high-redshift ($z \gtrsim 2$) star-forming galaxies (SFGs) have (1) higher molecular gas-to-stellar mass ratios ($\mu_{\text{gas}} \equiv M_{\text{mol}}/M_{*}$) and (2) shorter molecular gas depletion times ($\tau_{\text{dep}} \equiv M_{\text{mol}}/\text{SFR}$) than local galaxies (e.g., Tacconi et al. 2020).

Low- J CO transitions probe the cold and diffuse molecular gas, whereas mid- J transitions¹⁶ probe the warm and dense

regions of the molecular gas. Based on zoomed-in cosmological hydrodynamical simulations implementing radiative transfer calculations, Vallini et al. (2019) showed that galaxies in the epoch of reionization (EoR; $z \gtrsim 6$) have high gas excitation conditions with CO luminosity peaks at an upper rotational level (J_{u}) $\approx 6\text{--}7$ as a result of their high star formation surface density and the resulting higher temperature of the giant molecular clouds. These authors show that the sensitivity of the Atacama Large Millimeter/submillimeter Array (ALMA) telescope is sufficient to detect these mid- J CO transitions in a reasonable amount of integration time.

Observations of the low- J CO transitions in galaxies in the EoR are challenging because these transitions are redshifted to longer radio wavelengths, where instruments are less sensitive. Furthermore, at high redshift, the cosmic microwave background (CMB) has a significant impact upon the CO line emission (e.g., Combes et al. 1999; Sakamoto 1999; Papadopoulos et al. 2000; Obreschkow et al. 2009; da Cunha et al. 2013; Tunnard & Greve 2016; Zhang et al. 2016). First, the increased CMB heating leads to a greater population of high rotational levels, thereby boosting higher- J CO luminosities. Second, the CMB serves as a stronger background, particularly at the wavelength of the lower- J transitions. As a result, it

¹⁶ Hereafter, we refer to CO($J = 6 \rightarrow 5$) and CO($J = 7 \rightarrow 6$) as the mid- J transitions.



Table 1
Summary of Previous Measurements

Parameters	Measurements	References
$L_{\text{UV}} [L_{\odot}]$	2.0×10^{11}	B17
$L_{[\text{O III}]} [L_{\odot}]$	$(3.4 \pm 0.4) \times 10^9$	H19
$L_{[\text{C II}]} [L_{\odot}]$	$(1.1 \pm 0.1) \times 10^9$	H19
$L_{\text{TIR}} (T_d = 40 \text{ K}, \beta = 2.0) [L_{\odot}]$	4.0×10^{11}	S21
$L_{\text{TIR}} (T_d = 80 \text{ K}, \beta = 1.0) [L_{\odot}]$	12.6×10^{11}	S21
$L_{\text{FIR}} (T_d = 40 \text{ K}, \beta = 2.0) [L_{\odot}]$	3.1×10^{11}	...
$L_{\text{FIR}} (T_d = 80 \text{ K}, \beta = 1.0) [L_{\odot}]$	5.3×10^{11}	...

Note. The upper limit is 3σ . The total-infrared luminosity, L_{TIR} , and FIR luminosity, L_{FIR} , are estimated by integrating the modified blackbody radiation at 8–1000 and 42.5–122.5 μm , respectively. Following Sugahara et al. (2021), we consider two combinations of $(T_d, \beta) = (40 \text{ K}, 2.0)$ and $(80 \text{ K}, 1.0)$. B17, H19, and S21 refer to the studies by Bowler et al. (2017), Hashimoto et al. (2019), and Sugahara et al. (2021), respectively.

becomes challenging to observe low- J CO compared to the mid- J transitions at high redshift. Hence, to efficiently detect the molecular gas component, we target the brighter mid- J transitions, which can be observed far more efficiently with (sub)millimeter facilities.

The $[\text{C I}] \ ^3P_1 \rightarrow \ ^3P_0$ and $[\text{C I}] \ ^3P_2 \rightarrow \ ^3P_1$ lines could be more reliable tracers of the bulk of cold gas than mid- and even low- J transitions, particularly under certain conditions (e.g., high cosmic-ray flux, low metallicity). For example, Weiß et al. (2005), Offner et al. (2014), and Glover et al. (2015) showed that $[\text{C I}]$ is optically thin and traces the surfaces of molecular clouds in a range of environments (e.g., Shimajiri et al. 2013; Papadopoulos et al. 2018; Jiao et al. 2019).

To date, CO line observations in the EoR were mainly focused on dusty star-forming galaxies (DSFGs) and quasar host galaxies that both have high IR luminosities ($L_{\text{IR}} \gtrsim 10^{12} - 10^{13} L_{\odot}$) and large star formation rates (SFRs) $\gtrsim 100 - 1000 M_{\odot} \text{ yr}^{-1}$. Among the DSFGs at $z > 5$, seven sources were detected in the low- J CO line ($J_{\text{up}} = 1, 2$; Combes et al. 2012; Riechers et al. 2013, 2020, 2021; Rawle et al. 2014; Pavesi et al. 2018; Zavala et al. 2022), and more than 11 sources were detected in the mid- J CO line ($J_{\text{up}} \sim 6 - 7$; Combes et al. 2012; Riechers et al. 2013, 2017, 2020; Vieira et al. 2013, 2022; Rawle et al. 2014; Asboth et al. 2016; Strandet et al. 2016, 2017; Zavala et al. 2018; Apostolovski et al. 2019; Casey et al. 2019; Jin et al. 2019; Jarugula et al. 2021). Among the quasar host galaxies at $z \gtrsim 6$, at least eight sources were detected in the low- J CO line (Wang et al. 2010, 2011a, 2016; Stefan et al. 2015; Venemans et al. 2017a; Shao et al. 2019), and more than 25 sources were detected in the mid- J CO line (e.g., Walter et al. 2003; Riechers et al. 2009; Wang et al. 2011b, 2016, 2019; Carilli & Walter 2013; Venemans et al. 2017a, 2017b; Novak et al. 2019; Yang et al. 2019; Li et al. 2020; Decarli et al. 2022). In contrast, among “normal” SFGs at $z \sim 6$, only one source was detected in the low- J CO line (Pavesi et al. 2019), and two sources were detected in the CO($J = 6 \rightarrow 5$) line (D’Odorico et al. 2018; Vieira et al. 2022).

It is therefore of interest to investigate the nature of the molecular gas in B14-65666 (“Big Three Dragons”¹⁷) at $z = 7.1520$. This galaxy shows no clear signs of active galactic nucleus (AGN) activity; nonetheless, it is one of the brightest

LBGs at $z \gtrsim 6$ in the rest-frame ultraviolet (UV) continuum, far-IR (FIR) continuum, and FIR emission lines of $[\text{O III}] \ 88 \mu\text{m}$ and $[\text{C II}] \ 158 \mu\text{m}$ (Bowler et al. 2014; Furusawa et al. 2016; Hashimoto et al. 2019; Sugahara et al. 2021). The large IR and $[\text{C II}]$ luminosities imply the presence of a significant amount of dust and neutral gas, respectively, effectively shielding CO from the UV radiation. Previous studies have also shown that B14-65666 is an example of the highest- z starburst galaxies owing to a major merger event (Bowler et al. 2017; Hashimoto et al. 2019). Thus, a detailed study of the molecular gas in B14-65666 may provide information on the connection between mergers, starbursts, the emergence of quasars, and quenching of star formation at high redshift (e.g., Hopkins et al. 2008).

Herein, we present new ALMA Band 3 observations of B14-65666. Our observational setup efficiently covers CO($J = 6 \rightarrow 5$), CO($J = 7 \rightarrow 6$), and $[\text{C I}] \ ^3P_2 \rightarrow \ ^3P_1$. $[\text{C I}]$ is highly complementary to mid- J CO; it could trace the bulk of the cold molecular gas component without the need for low- J CO observations.

The rest of this paper is structured as follows. In Section 2, we introduce the target galaxy, B14-65666. In Section 3, we describe our ALMA Band 3 data. In Section 4, we calculate the line luminosities and estimate the molecular gas mass in the galaxy. In Section 5, we compare B14-65666 with other high- z objects in terms of the luminosity ratios and interstellar medium (ISM) properties. Section 6 presents discussions in the context of μ_{gas} and τ_{dep} . Finally, Section 7 presents our conclusions. Throughout this paper, magnitudes are given in the AB system (Oke & Gunn 1983), and we assume a Λ cold dark matter cosmology with $\Omega_m = 0.272$, $\Omega_b = 0.045$, $\Omega_{\Lambda} = 0.728$, and $H_0 = 70.4 \text{ km s}^{-1} \text{ Mpc}^{-1}$ (Komatsu et al. 2011). The solar luminosity, L_{\odot} , is $3.839 \times 10^{33} \text{ erg s}^{-1}$. Hereafter, we denote CO($J = 6 \rightarrow 5$), CO($J = 7 \rightarrow 6$), and $[\text{C I}] \ ^3P_2 \rightarrow \ ^3P_1$ as CO(6–5), CO(7–6), and $[\text{C I}](2-1)$, respectively.

2. Our Target: “Big Three Dragons”

Table 1 summarizes previous observations of the target. The galaxy was discovered by Bowler et al. (2014) based on wide-field imaging data of the UltraVISTA survey (e.g., McCracken et al. 2012). The galaxy has a UV absolute magnitude of $M_{\text{UV}} \approx -22.4$, which is $\sim 3-4$ times brighter than the characteristic UV magnitude at $z = 7$, $M_{\text{UV}}^* \approx -21.0$ (e.g., Bouwens et al. 2021). Subsequently, a high-angular-resolution image taken with the Hubble Space Telescope (HST) revealed that B14-65666 comprises two spatially distinct clumps in the rest-frame UV, indicating that the target is experiencing a merger event (Bowler et al. 2017).

The spectroscopic redshift of B14-65666 was obtained with the Faint Object Camera and Spectrograph on Subaru at $z = 7.17$ with $\text{Ly}\alpha$ (Furusawa et al. 2016). We performed ALMA spectroscopy of $[\text{O III}] \ 88 \mu\text{m}$ and $[\text{C II}] \ 158 \mu\text{m}$ and determined its spectroscopic redshift at 7.1520 ± 0.0003 (Hashimoto et al. 2019). Notably, Hashimoto et al. (2019) supported the merger interpretation by showing that $[\text{O III}]$ and $[\text{C II}]$ can be spatially decomposed into two components associated with the two UV clumps that are kinematically separated by $\approx 150 \text{ km s}^{-1}$. Furthermore, our team (Hashimoto et al. 2019; Sugahara et al. 2021) and Bowler et al. (2018, 2022) used ALMA to detect the dust continuum emission at $\lambda_{\text{rest}} \approx 90, 120$, and $160 \mu\text{m}$ with ALMA Bands 8, 7, and 6, respectively.

¹⁷ “Big Three Dragons” is a hand in a Mahjong game with triplets or quads of all three dragons.

Table 2
ALMA Band 3 Data

Data	Sensitivity ($\mu\text{Jy beam}^{-1}$)	Beam FWHM ($''$)	BPA ($^\circ$)
Without uv -taper			
Continuum	4.6	0.46×0.41	61
CO(6–5)	96	0.52×0.43	66
CO(7–6) and [C I](2–1)	78	0.43×0.37	66
uv -tapered			
Continuum	5.3	0.82×0.72	82
CO(6–5)	107	0.78×0.68	78
CO(7–6) and [C I](2–1)	93	0.78×0.68	78

Note. In uv -tapered data, we adopt taper values of $0''.45$, $0''.40$, and $0''.45$ for the continuum map, CO(6–5) cube, and CO(7–6) cube, respectively. The cube sensitivity is per 50 km s^{-1} .

With this large set of multiwavelength line and continuum measurements, B14-65666 has a well-sampled dust spectral energy distribution (SED). With modified blackbody radiation models for the dust continuum radiation, Sugahara et al. (2021) constrained the total-infrared luminosity (L_{TIR} ; integrated at $8-1000 \mu\text{m}$) to be 4.0 and $12.6 \times 10^{11} L_\odot$ with a parameter set of $(T_d, \beta) = (40 \text{ K}, 2.0)$ and $(80 \text{ K}, 1.0)$, respectively, where T_d and β are the dust temperature and emissivity index, respectively. In the calculation of L_{TIR} , the effect of the CMB is corrected following da Cunha et al. (2013).

3. ALMA Observations and Data Reduction

We performed ALMA Band 3 observations during 2019 September 17–22, as a Cycle 6 program (ID: 2018.1.01673.S, PI: T. Hashimoto). We used 41–45 antennas with baseline lengths of $15-2954 \text{ m}$, resulting in a maximum recoverable scale of $\sim 6''$. Four spectral windows were set at central frequencies of 85.00 , 86.88 , 97.15 , and 98.95 GHz , referred to as SPW1, SPW2, SPW3, and SPW4, respectively. The CO(6–5) line was observed in SPW1, and the CO(7–6) and [C I](2–1) lines were observed in SPW3. Continuum emission was observed in SPW2 and SPW4. The total on-source exposure time was 3.75 hr . The quasar J1008+0029 was used for complex gain calibration. Two quasars, J0854+2006 and J1037-2934, were used for bandpass calibration. The flux was scaled using J0854+2006 and J1037-2934, yielding an absolute accuracy below 5% in ALMA Band 3.

The data were reduced and calibrated with the Common Astronomy Software Application (CASA; McMullin et al. 2007) pipeline version 5.6.1-8. By using the `tclean` task, we produced maps and cubes with a natural weighting to optimize the point-source sensitivity. Table 2 summarizes the resulting resolution and sensitivity of the data.

Continuum maps were created using all channels that were expected to be line-free. The synthesized beam has a size of $0''.46 \times 0''.41$ in the FWHM and a positional angle (BPA) of 61° with an rms value of $4.6 \mu\text{Jy beam}^{-1}$. The beam size is smaller than the beam-deconvolved size of the target for the dust continuum and [C II] emitting region ($\sim 0''.8 \times 0''.4$ in FWHM; see Hashimoto et al. 2019). Therefore, we also created dust continuum maps using a Gaussian taper with a width ranging from $0''.0$ to $1''.0$. We adopted a taper value of $0''.45$ because the resultant beam size ($0''.82 \times 0''.72$) fully covers the dust continuum emitting region.

The data probe the dust continuum emission at $\lambda_{\text{rest}} \approx 400 \mu\text{m}$. The left panel of Figure 1 shows the nondetection, and by using the uv -tapered image, we place a 3σ upper limit of $15.9 \mu\text{Jy}$ on the continuum flux density. The current data is not deep enough to obtain a meaningful constraint on the dust emissivity index.

As the dust continuum was undetected in ALMA Band 3, we created line cubes without performing continuum subtraction. The cubes were rebinned to a velocity resolution of 50 km s^{-1} . For SPW1 (SPW3) targeting CO(6–5) [CO(7–6) and [C I](2–1)], we also created a uv -tapered data cube by using a Gaussian taper with a width of $0''.40$ ($0''.45$). This cube has a synthesized beam size of $0''.78 \times 0''.68$ ($0''.78 \times 0''.68$) and a typical sensitivity of 107 (93) $\mu\text{Jy beam}^{-1}$. Hereafter, we use the uv -tapered maps and cubes unless otherwise specified.

We have searched for the presence of emission lines in the cubes at the position of the target. At $z = 7.1520$, the CO(6–5), CO(7–6), and [C I](2–1) emission lines are expected to be at observed frequencies of 84.82 , 98.95 , and 99.28 GHz , respectively. Figure 1 also shows the integrated intensity maps (i.e., moment 0 maps) of CO(6–5), CO(7–6), and [C I](2–1). In these maps, we integrate the velocity range from -200 to $+200 \text{ km s}^{-1}$ with the CASA task `immoments`, which is comparable to the FWHM of [O III] and [C II] (Hashimoto et al. 2019).¹⁸ Figure 2 shows the spectra obtained in a $1''.5$ -diameter aperture centered on the target, where the large aperture size is adopted to capture possible spatially extended CO emission (Cicone et al. 2021). We conclude that the CO(6–5), CO(7–6), and [C I](2–1) lines are undetected.

4. Derived Properties

4.1. CO and [C I] Line Fluxes

From the integrated intensity maps, we obtain the 3σ upper limits on the velocity-integrated flux, $S_{\text{line}}\Delta v$, as 0.0581 , 0.0546 , and $0.0542 \text{ Jy km s}^{-1}$ for CO(6–5), CO(7–6), and [C I](2–1), respectively. Here we assumed that the size of the CO emitting region should not exceed that of the [C II] emission, which is a better tracer of more extended and multiphase gas. To obtain the intrinsic line fluxes, we correct for the impact of the CMB. Following Equation (32) of da Cunha et al. (2013), the fraction of the intrinsic line flux observed against the CMB is written as

$$f_{\text{CMB}} = \frac{S_{\nu/(1+z)}^{J_u[\text{obs against CMB}]}}{S_{\nu/(1+z)}^{J_u[\text{intrinsic}]}} = 1 - \frac{B_\nu[T_{\text{CMB}}(z)]}{B_\nu[T_{\text{exc}}]}, \quad (1)$$

where $S_{\nu/(1+z)}^{J_u[\text{intrinsic}]}$ and $S_{\nu/(1+z)}^{J_u[\text{obs against CMB}]}$ represent the intrinsic and observed flux density of the transition of J_u , respectively. $T_{\text{CMB}}(z) = (1+z) \times 2.73 \text{ K}$ is the CMB temperature at z , and T_{exc} is the excitation temperature in units of K. $B_\nu(T)$ is the Planck function. f_{CMB} can be estimated under the assumptions of the local thermal equilibrium (LTE) of molecular clouds and the thermal equilibrium of dust and gas (Goldsmith 2001). In this case, we can assume $T_{\text{exc}} = T_{\text{kin}} = T_{\text{dust}}$, where T_{kin} is the gas kinetic temperature. We estimate f_{CMB} to be $\sim 0.6-0.9$ using the dust temperature, $T_{\text{dust}} \sim 40-80 \text{ K}$, in the target (Sugahara et al. 2021). In the non-LTE case, f_{CMB} depends on a

¹⁸ Several studies show that CO(6–5) and [C II] have similar FWHMs (e.g., Wang et al. 2013, 2016; Strandet et al. 2017; Venemans et al. 2017b; Zavala et al. 2018).

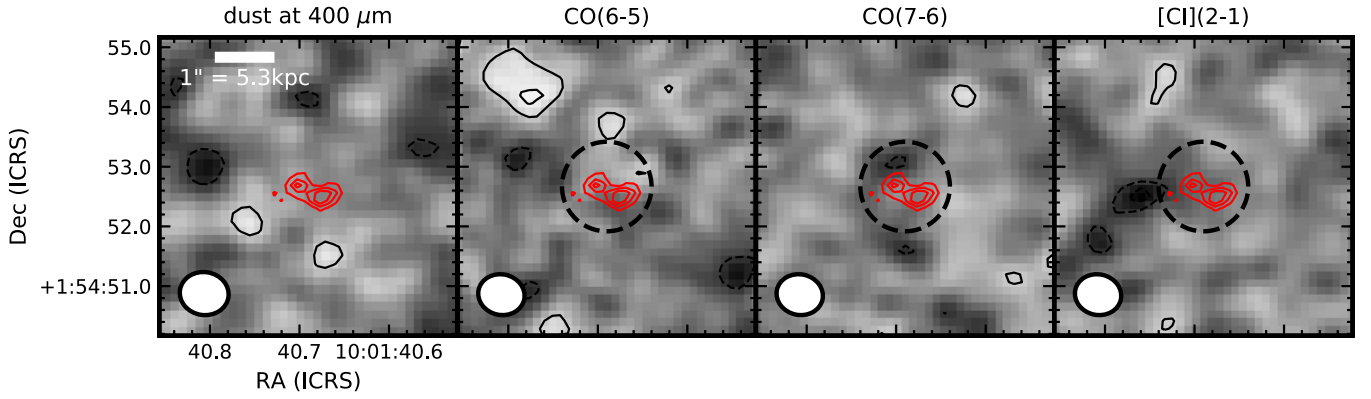


Figure 1. From left to right, $5''.0 \times 5''.0$ cutout images of dust continuum map and integrated intensity maps of CO(6–5), CO(7–6), and [C I](2–1). In each panel, red contours illustrate the morphology in the HST/WFC3 F140W band that probes the rest-frame UV continuum emission. Black contours are drawn at $(\pm 2, \pm 3) \times \sigma$, where the σ values are $\approx 5.3 \mu\text{Jy}$ for the dust continuum map, and 14.9, 14.0, and 13.9 mJy beam $^{-1}$ km s $^{-1}$ for the CO(6–5), CO(7–6), and [C I](2–1) maps, respectively. The black dashed circle at the center shows the $1''.5$ -diameter aperture used to extract the spectra in Figure 2. No significant emission has been detected.

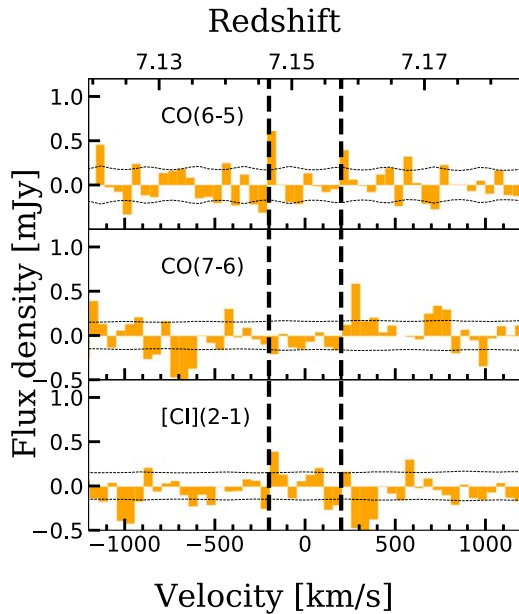


Figure 2. Top, middle, and bottom panel shows the spectrum of CO(6–5), CO(7–6), and [C I], respectively (units: millijanskys), as extracted from the $1''.5$ -diameter aperture indicated by the black dashed circle in Figure 1. The black dotted curve shows the noise spectrum. The vertical dashed line shows the velocity range from -200 to $+200$ km s $^{-1}$ that is used to create the integrated intensity maps in Figure 1, where the velocity zero-point is defined at $z = 7.152$ (Hashimoto et al. 2019). The velocity width is set to 50 km s $^{-1}$.

variety of parameters such as T_{kin} ; the number density of H $_2$ molecules, n_{H_2} ; and number density of CO molecules (da Cunha et al. 2013). Because the number of CO collisions with H $_2$ becomes small at low n_{H_2} , the mid- to high- J CO transitions with higher critical densities depart from the LTE case. This leads to $T_{\text{CMB}} \sim T_{\text{exc}} < T_{\text{kin}}$, and it could lead to f_{CMB} as small as 0.1 in the case of $T_{\text{exc}} = 23$ K (see Figure 8 in Combes et al. 1999). In summary, f_{CMB} is highly uncertain, ranging from ~ 0.1 – 0.9 at $T_{\text{exc}} = 23$ – 80 K.

4.2. Upper Limits on CO and [C I] Line Luminosities

We obtain the 3σ upper limits on two types of line luminosities (Solomon et al. 1992; Carilli & Walter 2013),

Table 3
Summary of Measurements

Parameters (1)	CO(6–5) (2)	CO(7–6) (3)	[C I](2–1) (4)
$S_{\text{line}}\Delta\nu$	<0.0581	<0.0546	<0.0542
$S_{\text{line}}\Delta\nu(\text{corr.})$	$<\frac{0.0581}{f_{\text{CMB}}}$	$<\frac{0.0546}{f_{\text{CMB}}}$	$<\frac{0.0542}{f_{\text{CMB}}}$
L_{line}	<2.70	<2.96	<2.95
$L_{\text{line}}(\text{corr.})$	$<\frac{2.70}{f_{\text{CMB}}}$	$<\frac{2.96}{f_{\text{CMB}}}$	$<\frac{2.95}{f_{\text{CMB}}}$
L'_{line}	<2.55	<1.77	<1.74
$L'_{\text{line}}(\text{corr.})$	$<\frac{2.55}{f_{\text{CMB}}}$	$<\frac{1.77}{f_{\text{CMB}}}$	$<\frac{1.74}{f_{\text{CMB}}}$
$L_{[\text{O III}]} / L_{\text{line}}$	>125	>115	>115
$L_{[\text{O III}]} / L_{\text{line}}(\text{corr.})$	$>125f_{\text{CMB}}$	$>115f_{\text{CMB}}$	$>115f_{\text{CMB}}$
$L_{[\text{C II}]} / L_{\text{line}}$	>41	>37	>37
$L_{[\text{C II}]} / L_{\text{line}}(\text{corr.})$	$>41f_{\text{CMB}}$	$>37f_{\text{CMB}}$	$>37f_{\text{CMB}}$

Note. The limits correspond to 3σ . $S_{\text{line}}\Delta\nu$ is the line flux in units of jansky kilometer per second. L_{line} and L'_{line} are the line luminosities in units of $10^7 L_{\odot}$ and $10^9 \text{ K km s}^{-1} \text{ pc}^2$, respectively. The CMB-corrected values are shown with “(corr.),” where f_{CMB} ranges from 0.1–0.9 (see the main text).

which are summarized in Table 3. The first one, L_{line} in units of L_{\odot} , is written as

$$L_{\text{line}} = 1.04 \times 10^{-3} \times S_{\text{line}}\Delta\nu D_L^2 \nu_{\text{obs}}, \quad (2)$$

where $S_{\text{line}}\Delta\nu$ is the velocity-integrated flux in units of jansky kilometers per second, D_L is the luminosity distance in megaparsecs, and ν_{obs} is the observed frequency in gigahertz. The second one, L'_{line} , corresponds to the area-integrated brightness in units of $\text{K km s}^{-1} \text{ pc}^2$, and it is written as

$$L'_{\text{line}} = 3.25 \times 10^7 \times S_{\text{line}}\Delta\nu \frac{D_L^2}{(1+z)^3 \nu_{\text{obs}}^2}. \quad (3)$$

With $S_{\text{line}}\Delta\nu$ (Table 3), the 3σ upper limits on L_{line} (L'_{line}) are $\frac{2.70}{f_{\text{CMB}}}$, $\frac{2.96}{f_{\text{CMB}}}$, and $\frac{2.95}{f_{\text{CMB}}} \times 10^7 L_{\odot}$ ($\frac{2.55}{f_{\text{CMB}}}$, $\frac{1.77}{f_{\text{CMB}}}$, and $\frac{1.74}{f_{\text{CMB}}} \times 10^9 \text{ K km s}^{-1} \text{ pc}^2$) for CO(6–5), CO(7–6), and [C I](2–1), respectively.

Table 4
Molecular Gas Mass

Method	M_{mol} $10^{10} M_{\odot}$
CO(6–5)	<(40–300)
CO(7–6)	<(30–250)
[C I](2–1)	<(30–820)
[C II] 158 μm	5.4–23
Dust	0.05–17
Dynamical mass	<11

Note. The estimates based on mid- J CO and [C I](2–1) are 3σ upper limits, where the values in the parenthesis reflect the uncertainty in the CMB correction. The estimate based on the dynamical mass (M_{dyn}) provides the upper limit.

4.3. Molecular Gas Mass Estimates

We estimate the molecular gas mass of B14-65666. In light of the rich data set, we adopt five techniques as summarized in Table 4.

4.3.1. Estimates with CO(6–5) and CO(7–6)

The molecular gas mass is estimated with CO lines as

$$\frac{M_{\text{mol}}^{\text{CO}}}{M_{\odot}} = \alpha_{\text{CO}} r_{J1}^{-1} L'_{\text{CO}_{J-1}}, \quad (4)$$

where α_{CO} is the CO-to- H_2 conversion factor in units of $M_{\odot} (\text{K km s}^{-1})^{-1}$, and r_{J1} is the excitation correction factor defined as

$$r_{J1} = \frac{L'_{\text{CO}_{J-1}}}{L'_{\text{CO}_{1-0}}} = \frac{I_{\text{CO}_{J-1}}}{I_{\text{CO}_{1-0}}} \frac{1}{J^2}. \quad (5)$$

We use Equation (19) of Narayanan & Krumholz (2014), who have shown that the CO excitation ladders can be parameterized with Σ_{SFR} based on simulations of disk galaxies combined with CO line radiative transfer calculations. With $\Sigma_{\text{SFR}} = 20.6_{-7.6}^{+11.4} M_{\odot} \text{ yr}^{-1} \text{ kpc}^{-2}$ obtained for the target,¹⁹ $r_{61} = 0.28_{-0.02}^{+0.04}$ and $r_{71} = 0.17_{-0.02}^{+0.02}$. With the upper limit on the CO(7–6) luminosity (Table 3), we obtain $L'_{\text{CO}_{J=1-0}} < \frac{1.2 \times 10^{10}}{f_{\text{CMB}}} \text{ K km s}^{-1} \text{ pc}^2$ (3σ).

Previous observational studies (e.g., Leroy et al. 2011; Shi et al. 2016) as well as theoretical ones (e.g., Wolfire et al. 2010; Narayanan et al. 2012) show that α_{CO} increases at lower gas-phase metallicity as a result of increased CO photodissociation. In this study, we adopt the conversion factor of Tacconi et al. (2018; their Equation (2)), which is a function of the gas-phase metallicity. The gas-phase metallicity of B14-65666 is estimated to be $0.4_{-0.2}^{+0.4} Z_{\odot}$ based on SED fits by taking into account the multiwavelength data ranging from rest-frame UV to FIR (Hashimoto et al. 2019). With a broad range of $0.2\text{--}0.8 Z_{\odot}$ (i.e., $12 + \log(\text{O}/\text{H}) = 8.0\text{--}8.6$), $\alpha_{\text{CO}} \approx 5\text{--}25 M_{\odot} (\text{K km s}^{-1} \text{ pc}^2)^{-1}$.

With $\alpha_{\text{CO}} = 25 M_{\odot} (\text{K km s}^{-1} \text{ pc}^2)^{-1}$ and the 3σ upper limit on $L'_{\text{CO}_{J=1-0}}$, we estimate the molecular gas mass to be $M_{\text{mol}}^{\text{CO}} < \frac{3.0 \times 10^{11}}{f_{\text{CMB}}} M_{\odot}$ (3σ). With $f_{\text{CMB}} \sim 0.1\text{--}0.9$, the 3σ upper

limit becomes $\sim(4\text{--}30) \times 10^{11} M_{\odot}$. Similarly, we obtain the 3σ upper limit of $(3\text{--}25) \times 10^{11} M_{\odot}$ from CO(6–5).

4.3.2. Estimate with [C I](2–1)

The neutral carbon mass, $M_{\text{C I}}$, can be obtained from the [C I] luminosity and T_{exc} . We estimate $M_{\text{C I}}$ following Weiß et al. (2003) as

$$\frac{M_{\text{C I}}}{M_{\odot}} = 4.566 \times 10^{-4} Q(T_{\text{exc}}) \frac{1}{5} e^{62.5/T_{\text{exc}}} \frac{L'_{[\text{C I}](2-1)}}{f_{\text{CMB}}}, \quad (6)$$

where $Q(T_{\text{exc}}) = 1 + 3e^{-T_1/T_{\text{exc}}} + 5e^{-T_2/T_{\text{exc}}}$ is the [C I] partition function, and $T_1 = 23.6 \text{ K}$ and $T_2 = 62.5 \text{ K}$ is the temperature of each transition from the ground state. By using $f_{\text{CMB}} \sim 0.1\text{--}0.9$ at $T_{\text{exc}} \sim 23\text{--}80 \text{ K}$ and the CMB-corrected luminosity of [C I](2–1), we obtain $M_{\text{C I}} < (2.2\text{--}59) \times 10^6 M_{\odot}$ (3σ). Assuming the abundance ratio of $X[\text{C I}]/X[\text{H}_2] \sim 1.6 \times 10^{-5}$ as obtained in $z \sim 1$ main-sequence galaxies (Valentino et al. 2018), the [C I](2–1)-based molecular gas mass is $M_{\text{mol}}^{[\text{C I}]} < (3.0\text{--}82) \times 10^{10} M_{\odot}$ (3σ), where the contribution of helium is included. Heintz & Watson (2020) revealed that the mass conversion factor of the [C I](1–0) transition, $\alpha_{[\text{C I}](1-0)} \equiv M_{\text{mol}}/L'_{[\text{C I}](1-0)}$, depends on the metallicity based on observations of [C I]($J=1$)²⁰ absorption lines in the rest-frame UV toward a sample of gamma-ray burst and quasar absorption systems at $z \sim 1.9\text{--}3.4$. $\alpha_{[\text{C I}](1-0)}$ becomes approximately 10 times higher at $0.2 Z_{\odot}$ than at Z_{\odot} . If we assume that the mass conversion factor of [C I](2–1) similarly changes with metallicity, our upper limits can be higher by a factor of 10, $M_{\text{mol}}^{[\text{C I}]} \lesssim (3.0\text{--}82) \times 10^{11} M_{\odot}$ (3σ) (Table 4).

4.3.3. Estimate with [C II] 158 μm

The [C II] 158 μm line can also be used to probe the molecular gas mass (Zanella et al. 2018; Dessauges-Zavadsky et al. 2020; Madden et al. 2020 and references therein). We use the conversion factor $\alpha_{[\text{C II}]}$ of Madden et al. (2020; see their Equation (5)) that is appropriate for metal-poor galaxies.

We apply two corrections to the [C II] luminosity. First, we remove the [C II] contribution originating from the HII region, although it becomes negligible in galaxies with, for example, low- Z (e.g., Croxall et al. 2017). From the metallicity of the target and Figure 9 of Cormier et al. (2019), we estimate the contribution from the HII region to be $\approx 30\%$. Second, we correct for the CMB impact to [C II]. Based on semianalytical model of galaxy formation combined with photoionization modeling, Lagache et al. (2018) showed that the [C II] luminosity can be reduced by 0.3 dex ($f_{\text{CMB}} = 0.5$) at $z = 7$ (see their Figure 4) in the case of a photodissociated region (PDR) with the hydrogen nuclei density of $\log(n(\text{H})) = 2.4$ irradiated by the incident FUV radiation field of $3.2 \times 10^3 G_0$, where G_0 is the Habing Field in unit, $1.6 \times 10^{-3} \text{ erg cm}^{-2} \text{ s}^{-1}$ (Habing 1968). These PDR parameters are similar to those obtained in $z \sim 3\text{--}4$ DSFGs (e.g., Wardlow et al. 2017), and are not improbable for B14-65666. Similarly, based on the cosmological hydrodynamic simulations combined with radiative transfer calculations, Vallini et al. (2015) also modeled the [C II] emission at $z \sim 7$ taking the CMB effect into account. These authors found that the [C II] emission from the PDR is

¹⁹ The target has $\text{SFR} = 200_{-32}^{+82} M_{\odot} \text{ yr}^{-1}$ and the [O III] beam-deconvolved size of $(3.8 \pm 0.5) \times (2.2 \pm 0.6) \text{ kpc}^2$ in FWHM (Hashimoto et al. 2019). The Σ_{SFR} value is calculated as $\frac{\text{SFR}}{2\pi r^2}$, where r is the half-light radius.

²⁰ J refers to the total angular momentum quantum number for this transition.

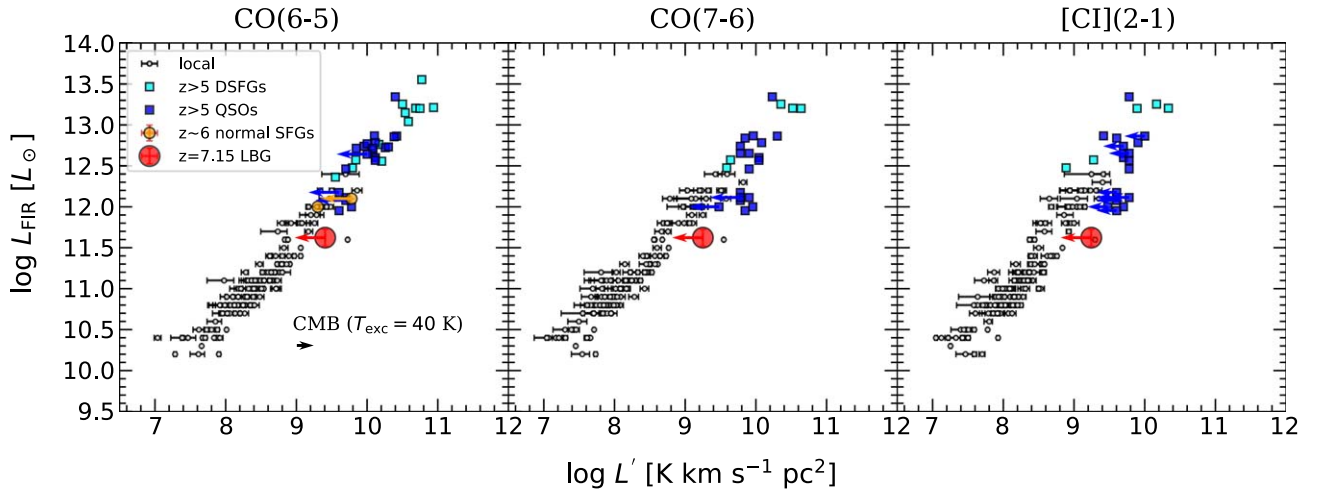


Figure 3. Far-IR luminosity defined in the range of 42.5–122.5 μm plotted against the line luminosity. The red circle, cyan squares, blue squares, and orange circles show the data points of B14-65666, $z > 5$ DSFGs, quasar host galaxies, and normal SFGs (see the text for the details of the literature sample), respectively, where the upper limits correspond to 3σ . For the detections at $z > 5$, the typical significance levels are 7, 6, and 4 for CO(6–5), CO(7–6), and [C I](2–1), corresponding to the line luminosity uncertainties of 0.1, 0.1, and 0.2 dex, respectively. The line luminosities are before the CMB correction. The black arrow in the left panel shows the impact of CMB at $T_{\text{exc}} = 40$ K; it shifts the data points toward higher line luminosities by ~ 0.2 dex at $z = 7$. Small open circles show a compilation of local objects, including SFGs, AGNs, and U/LIRGs observed with Herschel/SPIRE (Kamenetzky et al. 2016), where objects with $>3\sigma$ detections are plotted.

not severely impacted by the CMB effect, only up to 20% (see similar results in Kohandel et al. 2019). Given the uncertainty, we assume $f_{\text{CMB}} = 0.5 - 1.0$ in B14-65666. The intrinsic [C II] luminosity from the molecular gas is $\approx (7.7 - 17) \times 10^8 L_{\odot}$. We thus obtain $M_{\text{mol}}^{[\text{C II}]} \approx (5.4 - 23) \times 10^{10} M_{\odot}$, where we include the helium contribution and take into account a standard deviation of 0.14 dex in the relation.

4.3.4. Estimate with Dust Continuum

We estimate the gas mass based on M_d and the metallicity-dependent dust-to-gas ratio (DGR; Rémy-Ruyer et al. 2014; Li et al. 2019). With the prescription of Li et al. (2019) derived from cosmological hydrodynamical simulations implementing the process of dust production, growth, and destruction (see their Equation (9)), we obtain $\text{DGR} \approx (1.8 - 53) \times 10^{-4}$ at the metallicity of the target. Combined with the dust mass of the target, $\log(M_{\text{dust}}/M_{\odot}) \approx 6.4 - 7.5$ (Sugahara et al. 2021), we estimate the (molecular + atomic) gas mass to be $M_{\text{gas}}^{\text{dust}} \approx (0.05 - 17) \times 10^{10} M_{\odot}$. If we assume that gas is predominantly in the molecular phase (Riechers et al. 2013), this can be regarded as the molecular gas mass.

4.3.5. Upper Limit with Dynamical Mass

We calculate an upper limit on M_{mol} from the dynamical mass, M_{dyn} , subtracted by the stellar mass contribution. Hashimoto et al. (2019) obtained M_{dyn} of two individual clumps of B14-65666 based on the line width and beam-deconvolved size of [C II] 158 μm under the assumption of the virial theorem. The dynamical mass of the whole system is estimated to be $M_{\text{dyn}} = (8.8 \pm 1.9) \times 10^{10} M_{\odot}$, where the error only considers the measurement uncertainties. With a stellar mass obtained from SED fitting ($M_{\star} = 7.7_{-0.8}^{+1.0} \times 10^8 M_{\odot}$; Hashimoto et al. 2019), we obtain a conservative upper limit on M_{mol} to be $\sim 11 \times 10^{10} M_{\odot}$.

To summarize, by combining the M_{mol} estimates from the [C II] luminosity, dust mass, and dynamical mass, we obtain $M_{\text{mol}} = (0.05 - 11) \times 10^{10} M_{\odot}$, which is consistent with the upper limits on M_{mol} inferred from the nondetections of mid- J

CO and [C I](2–1). Although the Band 3 observations were conducted to constrain M_{mol} in B14-65666, we note that the tightest constraint on M_{mol} comes from the previous observations of dust and [C II] 158 μm , not from mid- J CO or [C I](2–1), due to the insufficient sensitivity of the Band 3 observations. Future deeper Band 3 observations are crucial to better constrain M_{mol} with mid- J CO or [C I](2–1).

5. Results

5.1. Luminosity Comparisons

5.1.1. Mid- J CO and [C I] versus Far-IR Luminosity

In the local universe, a compiled sample of SFGs, AGNs, and ultra/luminous infrared galaxies (U/LIRGs) observed by Herschel/SPIRE shows a positive correlation between the mid- J CO and the [C I](2–1) line luminosities and FIR luminosity, L_{FIR} (e.g., Kamenetzky et al. 2016). Figure 3 shows a comparison of B14-65666 with the local objects (Kamenetzky et al. 2016). The FIR luminosity of B14-65666 is calculated by integrating the modified blackbody radiation at 42.5–122.5 μm , where the CMB effect is corrected following da Cunha et al. (2013; Table 1). $z \sim 5 - 7$ DSFGs (Combes et al. 2012; Riechers et al. 2013, 2017, 2020; Zavala et al. 2018; Apostolovski et al. 2019; Casey et al. 2019; Jarugula et al. 2021; Vieira et al. 2022), quasar host galaxies (Riechers et al. 2009; Venemans et al. 2017a, 2017b; Novak et al. 2019; Wang et al. 2019; Yang et al. 2019; Decarli et al. 2022), as well as $z \sim 6$ normal SFGs (D’Odorico et al. 2018; Vieira et al. 2022) are also plotted, where the lensing magnification is corrected when necessary. Note that the number of data points differs in each transition. Although we show the line luminosities not corrected for the impact of the CMB, it shifts the line luminosities toward higher values by 0.2 dex at $T_{\text{exc}} = 40$ K at $z = 7$, as indicated by a black arrow in the left panel. Figure 3 shows that high- z sources also seem to follow the correlations. This might imply that the CMB effect may not be severe even at high redshift, although this could be due to a bias toward bright DSFGs and quasar host galaxies with higher T_{exc} .

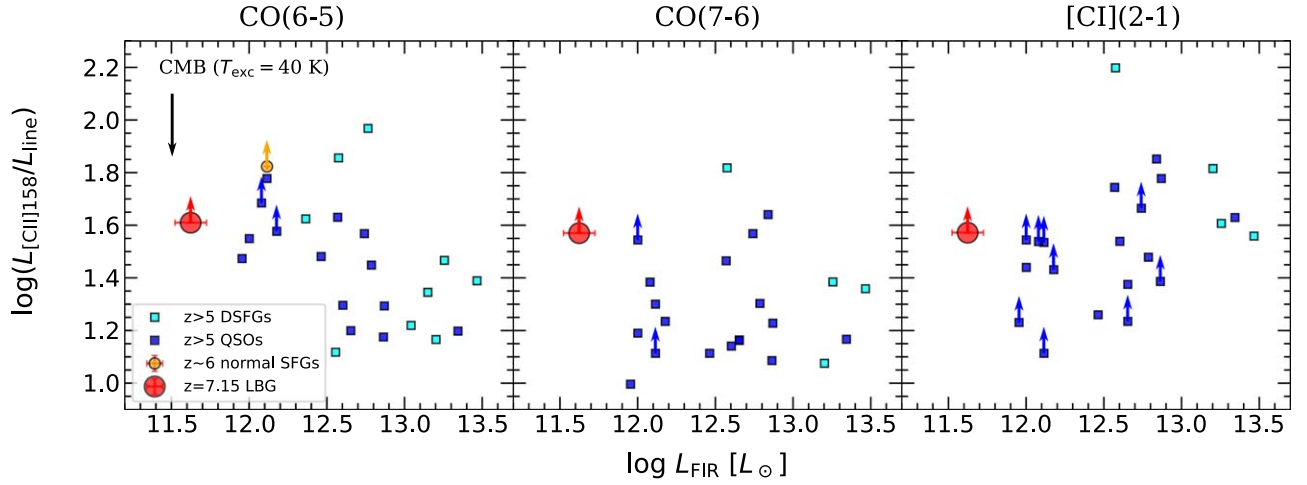


Figure 4. From left to right, $L_{[\text{C II}]} / L_{\text{CO}(6-5)}$, $L_{[\text{C II}]} / L_{\text{CO}(7-6)}$, and $L_{[\text{C II}]} / L_{[\text{C I}](2-1)}$ are plotted against L_{FIR} . The red circle, cyan squares, blue squares, and orange circles show the data points of B14-65666, $z > 5$ DSFGs, quasar host galaxies, and normal SFGs, respectively, where the upper limits correspond to 3σ . The line luminosities are before the CMB correction. The black arrow in the left panel shows the impact of the CMB on the lines at $T_{\text{exc}} = 40$ K; it shifts the data points toward lower line luminosity ratios by ~ -0.2 dex at $z = 7$.

The data points of B14-65666 for the first time place constraints on the line luminosities at $\log(L_{\text{FIR}}/L_{\odot}) < 12.0$ at $z > 6$. Nevertheless, the upper limits are loose at a given L_{FIR} , especially when the CMB impact is taken into account. This indicates that the nondetection of the lines can be explained by the insufficient sensitivity of the observations.

5.1.2. Mid-J CO and [C I] versus [C II] 158 μm Luminosity

Figure 4 shows plots of $L_{[\text{C II}]} / L_{\text{CO}(6-5)}$, $L_{[\text{C II}]} / L_{\text{CO}(7-6)}$, and $L_{[\text{C II}]} / L_{[\text{C I}](2-1)}$ against L_{FIR} . It also shows plots of DSFGs, quasar host galaxies, and normal SFGs at $z > 5$, with the luminosity measurements as in Figure 3. The luminosities are before the CMB correction.

B14-65666 has line luminosity ratios $\gtrsim 40$ (3σ). If we focus on $L_{[\text{C II}]} / L_{\text{CO}(7-6)}$, the lower limit is three times higher than the predicted value of ~ 13 for a simulated galaxy at $z = 6$ in Vallini et al. (2019), namely, “Althæa,” for which $M_{*} \approx 10^{10} M_{\odot}$, $\text{SFR} \approx 100 M_{\odot} \text{ yr}^{-1}$, and $Z \sim 0.5 Z_{\odot}$. B14-65666 has similar SFR and metallicity values; however, its stellar mass is approximately 1 order of magnitude lower than that of Althæa. Although only five (three) objects have $L_{[\text{C II}]} / L_{\text{CO}(6-5)}$ ($L_{[\text{C II}]} / L_{\text{CO}(7-6)}$) measurements higher than B14-65666, its interpretation is complicated owing to the large uncertainty in f_{CMB} . If B14-65666 has low n_{H_2} and/or gas temperature compared with those of DSFGs or quasar host galaxies at similar redshifts, f_{CMB} in B14-65666 becomes small, making the lower limits of B14-65666 more consistent with the typical values in high- z DSFGs and quasar host galaxies. Because a large fraction of the data points in Figure 4 comes from quasar host galaxies, the difficulty in measuring their stellar mass, size, and SFR surface densities also prevents us from further examining the physical origins of why B14-65666 has higher luminosity ratios than other EoR sources. The situation will be improved by the James Webb Space Telescope that provides these measurements in quasar host galaxies.

In summary, the current data is insufficient to examine the difference in the CMB-corrected $L_{[\text{C II}]} / L_{\text{line}}$ in B14-65666 and other high- z objects. The results also imply that care must be taken when comparing the luminosity ratios of galaxies in the EoR.

5.2. PDR Modeling

The luminosity ratios are useful to examine properties of the ISM (e.g., Kaufman et al. 2006; Pound & Wolfire 2008), although the impact of the CMB makes the interpretation complicated, as stated in Section 5.1.2. The $L_{[\text{C II}]} / L_{[\text{C I}](2-1)}$ luminosity ratio is sensitive to the heating source of the ISM (Meijerink et al. 2007). The high ratio, $\gtrsim 40$, excludes the possibility that the lines are heated by the X-ray dominated regions, where $L_{[\text{C II}]} / L_{[\text{C I}](2-1)} \lesssim 6$ is expected. We thus compare the line ratios of B14-65666 to the model predictions of PDR Toolbox (version wk2020) to place constraints on the physical properties of the PDRs. The model assumes a geometry of infinite plane slabs of hydrogen characterized by the hydrogen nuclei density, $n(\text{H})$, and the strength of the incident FUV radiation field, G , normalized to the Habing Field in units of $G_0 = 1.6 \times 10^{-3} \text{ erg cm}^{-2} \text{ s}^{-1}$. In a more realistic geometry of spherical clouds, the optically thin emission would be detected from both the front and back sides of the cloud, whereas the optically thick emission would be detected only from the front side (Yang et al. 2019). We therefore divide the luminosities of optically thin emission by a factor of 2. We also assume that the [C II] contribution from the PDR is 70% (Section 4.3.3). We adopt the line ratios before the correction of the CMB and discuss its impact later.

In Figure 5, the overlapped region of the four luminosity ratios is $\log(n(\text{H})/\text{cm}^{-3}) \sim 1-5$ with a moderate FUV radiation field $\sim 10^2-10^3 G_0$. The high $L_{[\text{C II}]} / L_{\text{CO}(6-5)}$ and $L_{[\text{C II}]} / L_{\text{CO}(7-6)}$ ratios exclude the possibility of $\log(n(\text{H})/\text{cm}^{-3}) > 5$. The strength of the incident FUV radiation field in B14-65666 is comparable to those in local (U)LIRGs and high- z DSFGs that have $\sim 10^2-10^4 G_0$, as indicated by the gray box in Figure 5 (Hughes et al. 2017; Wardlow et al. 2017), but lower than that of a $z \sim 6$ DSFG, G09.83808, with an FUV radiation field $\sim 10^4 G_0$ (cyan ellipse; Rybak et al. 2020). The gas density in B14-65666 is barely constrained, although it is lower than that obtained in some $z \sim 6-7$ quasar host galaxies (blue square: Shao et al. 2019).

The CMB effect makes the intrinsic $L_{[\text{C II}]} / L_{\text{CO}(6-5)}$, $L_{[\text{C II}]} / L_{\text{CO}(7-6)}$, and $L_{[\text{C II}]} / L_{[\text{C I}](2-1)}$ ratios lower because [C II] is less affected by the CMB compared to CO(6-5),

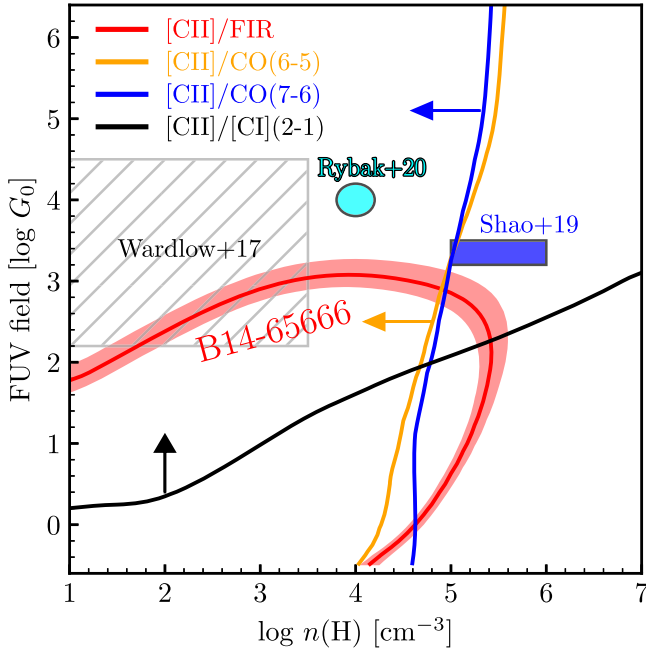


Figure 5. The FUV radiation field, G , and the hydrogen gas density, $n(\text{H})$, in B14-65666 as estimated using PDRToolbox (Pound & Wolfire 2008). The red line with a shaded region indicates the parameter space allowed by $L_{[\text{C II}]} / L_{\text{FIR}}$ and its uncertainty. The orange, blue, and black lines with arrows show the permitted ranges of parameters given by the 3σ lower limits on $L_{[\text{C II}]} / L_{\text{CO}(6-5)}$, $L_{[\text{C II}]} / L_{\text{CO}(7-6)}$, and $L_{[\text{C II}]} / L_{[\text{C I}](2-1)}$, respectively. The allowed parameter space of B14-65666 corresponds to the red line and shaded region left of the blue and yellow lines. B14-65666 has $\log(n(\text{H})/\text{cm}^{-3}) \sim 1-5$ and $\sim 10^2-10^3 G_0$. The results of other DSFGs at $z = 1-5$ (Wardlaw et al. 2017), a DSFG at $z = 6.0$ (Rybak et al. 2020), and three IR-bright quasar host galaxies at $z \sim 6$ (Shao et al. 2019) are also shown.

CO(7–6), and [C I]. The net effect is that the constraints on $n(\text{H})$ and G become weaker. The high luminosity ratios >40 (3σ) (Figure 4) may imply that the nondetection of the lines in B14-65666 could be partly due to its low $n(\text{H})$ compared to that of other high- z objects; however, the CMB effect prevents us from obtaining a conclusion.

5.3. Gas Fractions and Depletion Timescales

Despite the large uncertainty in M_{mol} (Section 4.3), we examine two physical quantities related with the molecular gas. The first one is the gas depletion time, $\tau_{\text{dep}} \equiv M_{\text{mol}}/\text{SFR}$. With $M_{\text{mol}} = 200^{+82}_{-38} M_{\odot} \text{ yr}^{-1}$ from SED fitting (Hashimoto et al. 2019), we obtain $\tau_{\text{dep}} \approx 2.5 - 550$ Myr. The second one is the molecular gas-to-stellar mass ratio, $\mu_{\text{gas}} \equiv M_{\text{mol}}/M_{*}$. With $M_{\text{mol}} = (0.05 - 11) \times 10^{10} M_{\odot}$ and the stellar mass obtained from SED fitting (Hashimoto et al. 2019), $M_{*} = 7.7^{+1.0}_{-0.8} \times 10^8 M_{\odot}$, we obtain $\mu_{\text{mol}} \approx 0.65 - 140$.

The left panel in Figure 6 shows a comparison of τ_{dep} of B14-65666 with other high- z objects shown in Figure 3 when the quantities are available. For the 12 data points of $z > 5$ DSFGs, we adopt τ_{gas} from the literature, if available. If not, we compute them from M_{mol} and SFRs. For the 10 quasar host galaxies in Decarli et al. (2022), the width of the box plot corresponds to their redshift range, whereas the height corresponds to the 84th percentile of τ_{gas} . We also individually plot the $z = 7.54$ quasar (Novak et al. 2019) and three $z \sim 7$ quasars (Venemans et al. 2017b), where τ_{gas} values are computed based on the combinations of CO-based M_{mol} and SFR. We also plot normal SFGs on the main sequence at

$4 < z < 6$ (Dessauges-Zavadsky et al. 2020) and an individual value of the $z \sim 5.7$ LBG, HZ10 (Pavesi et al. 2019). From the figure, we find that B14-65666 is consistent with other high- z sources and the extrapolations of the scaling relation in Tacconi et al. (2020; black lines).

The right panel in Figure 6 shows a comparison of μ_{gas} . In $z > 5$ DSFGs, the values are taken from the literatures if available. If not, we compute them from the stellar and gas mass estimates. We do not include $z > 5$ quasar host galaxies because their stellar masses are not well constrained. Again, B14-65666 is consistent with other high- z sources and the extrapolations of the scaling relation in Tacconi et al. (2020).

6. Discussion

We obtain τ_{dep} of 2.5 and 550 Myr in the cases of $M_{\text{mol}} = 0.05$ and $11 \times 10^{10} M_{\odot}$, respectively. In the case of $\tau_{\text{dep}} = 550$ (2.5) Myr, the galaxy will consume the molecular gas as early as $z \approx 4.5$ (7), if the galaxy is not fueled by further accretion, whose final stellar mass is approximately 1×10^{11} (1×10^9) M_{\odot} . This implies that B14-65666 can evolve into a passive galaxy at $z \gtrsim 4$. To further examine this hypothesis, we compare the volume number density of galaxies like B14-65666 with that of $z \sim 3-4$ passive galaxies. The number density of galaxies like B14-65666 ($M_{\text{UV}} = -22.4$) is $\sim 1 \times 10^{-6} \text{ Mpc}^{-3}$ based on the bright-end of the UV luminosity function at $z \sim 7$ (Bowler et al. 2017; Harikane et al. 2022). The observed number density of $z \sim 3-4$ passive galaxies was recently compiled by Valentino et al. (2020); it is $\mathcal{O}(10^{-6}) - \mathcal{O}(10^{-5}) \text{ Mpc}^{-3}$ at $M_{*} \geq 4 \times 10^{10} M_{\odot}$. These authors have also derived the number density by analyzing the *Illustris* TNG cosmological simulation public release data (e.g., Springel et al. 2018). In the simulation, the volume number density of $z = 3.7$ passive galaxies is estimated to be $\mathcal{O}(10^{-6}) \text{ Mpc}^{-3}$ at $M_{*} \geq 4 \times 10^{10} M_{\odot}$. A broad agreement in the number densities may support the idea that moderate starburst galaxies at $z > 7$, such as B14-65666, could be ancestors of $z \sim 3-4$ passive galaxies (see Valentino et al. 2020).

7. Conclusion

We have presented results of ALMA Band 3 observations of CO(6–5), CO(7–6), and [C I](2–1) in B14-65666 (“Big Three Dragons”). The target was previously detected in Ly α , [O III] 88 μm , [C II] 158 μm , and the dust continuum in the EoR (Hashimoto et al. 2019), and it is one of the brightest LBGs at $z > 7$ without gravitational lensing (Table 1).

1. We do not detect CO(6–5), CO(7–6), and [C I](2–1) (Figures 1 and 2). The 3σ upper limit on the line luminosity is $\approx (2.7-3.0) \times 10^7 L_{\odot}$ [i.e., $(1.7-2.6) \times 10^9 \text{ K km s}^{-1} \text{ pc}^2$], which is approximately 40 times fainter than the [C II] 158 μm luminosity before the CMB correction.
2. By comparing the line luminosity upper limits with $z > 5$ sources such as DSFGs and quasar host galaxies, we find that the nondetections are likely due to (1) the insufficient sensitivity of the observations (Figure 3) or (2) possibly low hydrogen gas density in the PDR (Figure 4), although the uncertainty in the CMB impact makes the interpretation complicated.
3. We have estimated the molecular gas mass, M_{mol} , of B14-65666 based on five techniques: (1) mid- J CO

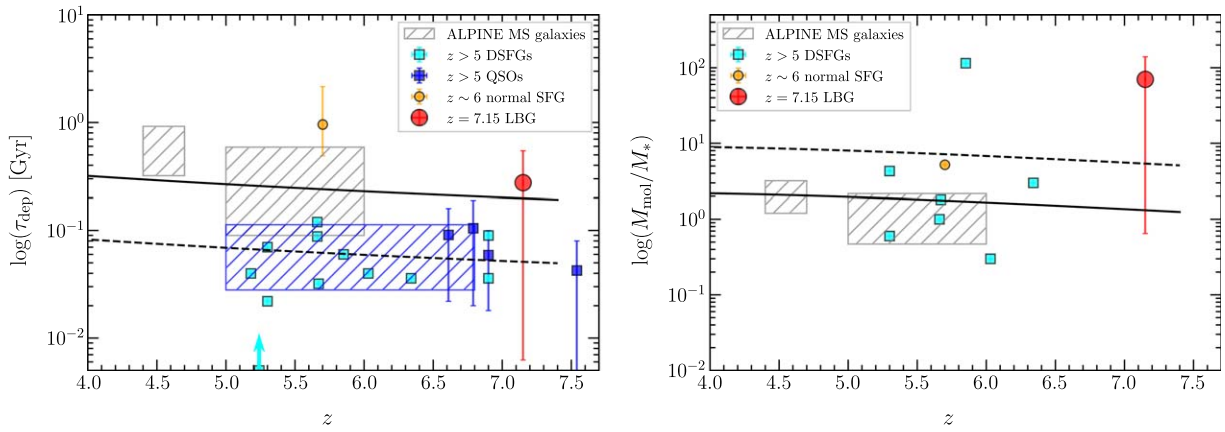


Figure 6. Evolution of the gas depletion time (τ_{dep}) and gas fraction (M_{mol}/M_*) at $z = 4 - 7.5$. (Left) The τ_{dep} value of B14-65666, indicated by the red circle, is compared against the values in 12 DSFGs at $z > 5$ (cyan squares), 10 quasar host galaxies at $z \sim 5 - 6.5$ (blue box regions), four quasar host galaxies at $z \sim 7$ (blue squares), a normal SFG at $z \sim 6$ (orange circle), and main-sequence galaxies at $z \sim 4.5 - 6.0$ (gray box regions). The solid and dashed lines indicate the scaling relations derived by Tacconi et al. (2020) for the main-sequence ($\log(\text{SFR}/\text{SFR}_{\text{MS}}) = 0$) and starburst galaxies ($\log(\text{SFR}/\text{SFR}_{\text{MS}}) = 1.2$) at $\log(M_*/M_\odot) = 10$, respectively, extrapolated to $z \sim 7$. (Right) Comparisons of M_{mol}/M_* in B14-65666 with those in high- z objects indicated by the same symbols as in the left panel.

luminosity, (2) [C I](2–1) luminosity, (3) [C II] 158 μm luminosity, (4) dust mass and a DGR, and (5) dynamical mass. From three methods, namely, [C II], dust mass, and dynamical mass, we obtain $M_{\text{mol}} = (0.05 - 11) \times 10^{10} M_\odot$, which is consistent with its upper limit inferred from the nondetection of mid- J CO and [C I](2–1) (Table 4).

4. By comparing the observed luminosities to the model predictions of the PDR, we find that B14-65666 has $\log(n(\text{H})/\text{cm}^{-3}) \sim 1-5$ with a moderate FUV radiation field of $\sim 10^2-10^3 G_0$. These values are broadly consistent with those obtained in local (U)LIRGs and high- z DSFGs/quasar host galaxies, although the constraints on $n(\text{H})$ and G can be weaker if the CMB effect is significant (Figure 5).
5. We estimate a molecular gas-to-stellar mass ratio (μ_{gas}) of 0.65–140 and a gas depletion time (τ_{dep}) of 2.5–550 Myr; these values are consistent with those of other high- z objects and the extrapolations of the scaling relations to $z \sim 7$ (Figure 6).
6. If the galaxy is not fueled by further accretion, we conjecture that B14-65666 could be an ancestor of $z \gtrsim 4$ passive galaxies; this is supported by the broad agreement of the number volume density of galaxies like B14-65666 and $z \sim 3 - 4$ passive galaxies.

Acknowledgments

We thank the anonymous referee for providing valuable comments that greatly improved this paper. T.H. was supported by Leading Initiative for Excellent Young Researchers, MEXT, Japan (HJH02007) and by JSPS KAKENHI grant Nos. 20K22358 and 22H01258. A.K.I., Y.S., and Y.F. are supported by NAOJ ALMA Scientific Research grant No. 2020-16B. A. K.I. acknowledges support from JSPS KAKENHI grant No. 23H00131. Y.T. acknowledges support from JSPS KAKENHI grant No. 22H04939. K.K. acknowledges support from the Knut and Alice Wallenberg Foundation. We thank Yoshito Shimajiri for support in analyzing ALMA data. We appreciate Hajime Fukushima, Shigeki Inoue, Satoshi Kikuta, Masami Ouchi, Hidenobu Yajima, and Atsuhiko Yasuda for discussion. We would like to thank Editage (www.editage.com) for English language editing. This paper makes use of the

following ALMA data: ADS/JAO.ALMA#2018.1.01673. ALMA is a partnership of ESO (representing its member states), NSF (USA), and NINS (Japan), together with NRC (Canada), MOST and ASIAA (Taiwan), and KASI (Republic of Korea), in cooperation with the Republic of Chile. The Joint ALMA Observatory is operated by ESO, AUI/NRAO, and NAOJ. The HST data used in this work are obtained through the data archive at the Space Telescope Science Institute, which is operated by the Association of Universities for Research in Astronomy, Inc. under NASA contract NAS 5-26555.

Facility: ALMA.

ORCID iDs

Takuya Hashimoto <https://orcid.org/0000-0002-0898-4038>
 Akio K. Inoue <https://orcid.org/0000-0002-7779-8677>
 Yuma Sugahara <https://orcid.org/0000-0001-6958-7856>
 Yoshinobu Fudamoto <https://orcid.org/0000-0001-7440-8832>
 Seiji Fujimoto <https://orcid.org/0000-0001-7201-5066>
 K. K. Knudsen <https://orcid.org/0000-0002-7821-8873>
 Hiroshi Matsuo <https://orcid.org/0000-0003-3278-2484>
 Yoichi Tamura <https://orcid.org/0000-0003-4807-8117>
 Satoshi Yamanaka <https://orcid.org/0000-0002-7738-5290>
 Yuichi Harikane <https://orcid.org/0000-0002-6047-430X>
 Nario Kuno <https://orcid.org/0000-0002-1234-8229>
 Yoshiaki Ono <https://orcid.org/0000-0001-9011-7605>
 Dragan Salak <https://orcid.org/0000-0002-3848-1757>

References

- Apostolovski, Y., Aravena, M., Anguita, T., et al. 2019, *A&A*, **628**, A23
 Asboth, V., Conley, A., Sayers, J., et al. 2016, *MNRAS*, **462**, 1989
 Bolatto, A. D., Wolfire, M., & Leroy, A. K. 2013, *ARA&A*, **51**, 207
 Bouwens, R. J., Oesch, P. A., Stefanon, M., et al. 2021, *AJ*, **162**, 47
 Bowler, R. A. A., Bourne, N., Dunlop, J. S., McLure, R. M., & McLeod, D. J. 2018, *MNRAS*, **481**, 1631
 Bowler, R. A. A., Cullen, F., McLure, R. J., Dunlop, J. S., & Avison, A. 2022, *MNRAS*, **510**, 5088
 Bowler, R. A. A., Dunlop, J. S., McLure, R. J., & McLeod, D. J. 2017, *MNRAS*, **466**, 3612
 Bowler, R. A. A., Dunlop, J. S., McLure, R. J., et al. 2014, *MNRAS*, **440**, 2810
 Carilli, C. L., & Walter, F. 2013, *ARA&A*, **51**, 105
 Casey, C. M., Zavala, J. A., Aravena, M., et al. 2019, *ApJ*, **887**, 55
 Ciccone, C., Mainieri, V., Circosta, C., et al. 2021, *A&A*, **654**, L8
 Combes, F., Maoli, R., & Omont, A. 1999, *A&A*, **345**, 369

- Combes, F., Rex, M., Rawle, T. D., et al. 2012, *A&A*, **538**, L4
- Cormier, D., Abel, N. P., Hony, S., et al. 2019, *A&A*, **626**, A23
- Croxall, K. V., Smith, J. D., Pellegrini, E., et al. 2017, *ApJ*, **845**, 96
- da Cunha, E., Groves, B., Walter, F., et al. 2013, *ApJ*, **766**, 13
- Decarli, R., Pensabene, A., Venemans, B., et al. 2022, *A&A*, **662**, A60
- Dessauges-Zavadsky, M., Ginolfi, M., Pozzi, F., et al. 2020, *A&A*, **643**, A5
- D’Odorico, V., Feruglio, C., Ferrara, A., et al. 2018, *ApJL*, **863**, L29
- Furusawa, H., Kashikawa, N., Kobayashi, M. A. R., et al. 2016, *ApJ*, **822**, 46
- Glover, S. C. O., Clark, P. C., Micic, M., & Molina, F. 2015, *MNRAS*, **448**, 1607
- Goldsmith, P. F. 2001, *ApJ*, **557**, 736
- Habing, H. J. 1968, *BAN*, **19**, 421
- Harikane, Y., Ono, Y., Ouchi, M., et al. 2022, *ApJS*, **259**, 20
- Hashimoto, T., Inoue, A. K., Mawatari, K., et al. 2019, *PASJ*, **71**, 71
- Heintz, K. E., & Watson, D. 2020, *ApJL*, **889**, L7
- Hopkins, P. F., Hernquist, L., Cox, T. J., & Kereš, D. 2008, *ApJS*, **175**, 356
- Hughes, T. M., Ibar, E., Villanueva, V., et al. 2017, *A&A*, **602**, A49
- Jarugula, S., Vieira, J. D., Weiss, A., et al. 2021, *ApJ*, **921**, 97
- Jiao, Q., Zhao, Y., Lu, N., et al. 2019, *ApJ*, **880**, 133
- Jin, S., Daddi, E., Magdis, G. E., et al. 2019, *ApJ*, **887**, 144
- Kamenetzky, J., Rangwala, N., Glenn, J., Maloney, P. R., & Conley, A. 2016, *ApJ*, **829**, 93
- Kaufman, M. J., Wolfire, M. G., & Hollenbach, D. J. 2006, *ApJ*, **644**, 283
- Kohandel, M., Pallottini, A., Ferrara, A., et al. 2019, *MNRAS*, **487**, 3007
- Komatsu, E., Smith, K. M., Dunkley, J., et al. 2011, *ApJS*, **192**, 18
- Lagache, G., Cousin, M., & Chatzikos, M. 2018, *A&A*, **609**, A130
- Leroy, A. K., Bolatto, A., Gordon, K., et al. 2011, *ApJ*, **737**, 12
- Li, J., Wang, R., Riechers, D., et al. 2020, *ApJ*, **889**, 162
- Li, Q., Narayanan, D., & Davé, R. 2019, *MNRAS*, **490**, 1425
- Madden, S. C., Cormier, D., Hony, S., et al. 2020, *A&A*, **643**, A141
- Magdis, G. E., Daddi, E., Béthermin, M., et al. 2012, *ApJ*, **760**, 6
- McCracken, H. J., Milvang-Jensen, B., Dunlop, J., et al. 2012, *A&A*, **544**, A156
- McMullin, J. P., Waters, B., Schiebel, D., Young, W., & Golap, K. 2007, in ASP Conf. Ser. 376, *Astronomical Data Analysis Software and Systems XVI*, ed. R. A. Shaw, F. Hill, & D. J. Bell (San Francisco, CA: ASP), **127**
- Meijerink, R., Spaans, M., & Israel, F. P. 2007, *A&A*, **461**, 793
- Narayanan, D., & Krumholz, M. R. 2014, *MNRAS*, **442**, 1411
- Narayanan, D., Krumholz, M. R., Ostriker, E. C., & Hernquist, L. 2012, *MNRAS*, **421**, 3127
- Novak, M., Bañados, E., Decarli, R., et al. 2019, *ApJ*, **881**, 63
- Obreschkow, D., Heywood, I., Klöckner, H. R., & Rawlings, S. 2009, *ApJ*, **702**, 1321
- Offner, S. S. R., Bisbas, T. G., Bell, T. A., & Viti, S. 2014, *MNRAS*, **440**, L81
- Oke, J. B., & Gunn, J. E. 1983, *ApJ*, **266**, 713
- Papadopoulos, P. P., Bisbas, T. G., & Zhang, Z.-Y. 2018, *MNRAS*, **478**, 1716
- Papadopoulos, P. P., Röttgering, H. J. A., van der Werf, P. P., et al. 2000, *ApJ*, **528**, 626
- Pavesi, R., Riechers, D. A., Faisst, A. L., Stacey, G. J., & Capak, P. L. 2019, *ApJ*, **882**, 168
- Pavesi, R., Sharon, C. E., Riechers, D. A., et al. 2018, *ApJ*, **864**, 49
- Pound, M. W., & Wolfire, M. G. 2008, in ASP Conf. Ser. 394, *Astronomical Data Analysis Software and Systems XVII*, ed. R. W. Argyle, P. S. Bunclark, & J. R. Lewis (San Francisco, CA: ASP), **654**
- Rawle, T. D., Egami, E., Bussmann, R. S., et al. 2014, *ApJ*, **783**, 59
- Rémy-Ruyer, A., Madden, S. C., Galliano, F., et al. 2014, *A&A*, **563**, A31
- Riechers, D. A., Bradford, C. M., Clements, D. L., et al. 2013, *Natur*, **496**, 329
- Riechers, D. A., Hodge, J. A., Pavesi, R., et al. 2020, *ApJ*, **895**, 81
- Riechers, D. A., Leung, T. K. D., Ivison, R. J., et al. 2017, *ApJ*, **850**, 1
- Riechers, D. A., Nayyeri, H., Burgarella, D., et al. 2021, *ApJ*, **907**, 62
- Riechers, D. A., Walter, F., Bertoldi, F., et al. 2009, *ApJ*, **703**, 1338
- Rybak, M., Zavala, J. A., Hodge, J. A., Casey, C. M., & Werf, P. v. d. 2020, *ApJL*, **889**, L11
- Sakamoto, S. 1999, *ApJ*, **523**, 701
- Scoville, N., Sheth, K., Aussel, H., et al. 2016, *ApJ*, **820**, 83
- Shao, Y., Wang, R., Carilli, C. L., et al. 2019, *ApJ*, **876**, 99
- Shi, Y., Wang, J., Zhang, Z.-Y., et al. 2016, *NatCo*, **7**, 13789
- Shimajiri, Y., Sakai, T., Tsukagoshi, T., et al. 2013, *ApJL*, **774**, L20
- Solomon, P. M., Downes, D., & Radford, S. J. E. 1992, *ApJL*, **398**, L29
- Springel, V., Pakmor, R., Pillepich, A., et al. 2018, *MNRAS*, **475**, 676
- Stefan, I. I., Carilli, C. L., Wagg, J., et al. 2015, *MNRAS*, **451**, 1713
- Strandet, M. L., Weiss, A., De Breuck, C., et al. 2017, *ApJL*, **842**, L15
- Strandet, M. L., Weiss, A., Vieira, J. D., et al. 2016, *ApJ*, **822**, 80
- Sugahara, Y., Inoue, A. K., Hashimoto, T., et al. 2021, *ApJ*, **923**, 5
- Tacconi, L. J., Genzel, R., Saintonge, A., et al. 2018, *ApJ*, **853**, 179
- Tacconi, L. J., Genzel, R., & Sternberg, A. 2020, *ARA&A*, **58**, 157
- Tunnard, R., & Greve, T. R. 2016, *ApJ*, **819**, 161
- Valentino, F., Magdis, G. E., Daddi, E., et al. 2018, *ApJ*, **869**, 27
- Valentino, F., Tanaka, M., Davidzon, I., et al. 2020, *ApJ*, **889**, 93
- Vallini, L., Gallerani, S., Ferrara, A., Pallottini, A., & Yue, B. 2015, *ApJ*, **813**, 36
- Vallini, L., Tielens, A. G. G. M., Pallottini, A., et al. 2019, *MNRAS*, **490**, 4502
- Venemans, B. P., Walter, F., Decarli, R., et al. 2017a, *ApJ*, **837**, 146
- Venemans, B. P., Walter, F., Decarli, R., et al. 2017b, *ApJ*, **845**, 154
- Vieira, D., Riechers, D. A., Pavesi, R., et al. 2022, *ApJ*, **925**, 174
- Vieira, J. D., Marrone, D. P., Chapman, S. C., et al. 2013, *Natur*, **495**, 344
- Walter, F., Bertoldi, F., Carilli, C., et al. 2003, *Natur*, **424**, 406
- Wang, F., Wang, R., Fan, X., et al. 2019, *ApJ*, **880**, 2
- Wang, R., Carilli, C. L., Neri, R., et al. 2010, *ApJ*, **714**, 699
- Wang, R., Wagg, J., Carilli, C. L., et al. 2011a, *ApJL*, **739**, L34
- Wang, R., Wagg, J., Carilli, C. L., et al. 2011b, *AJ*, **142**, 101
- Wang, R., Wagg, J., Carilli, C. L., et al. 2013, *ApJ*, **773**, 44
- Wang, R., Wu, X.-B., Neri, R., et al. 2016, *ApJ*, **830**, 53
- Wardlow, J. L., Cooray, A., Osage, W., et al. 2017, *ApJ*, **837**, 12
- Weiß, A., Henkel, C., Downes, D., & Walter, F. 2003, *A&A*, **409**, L41
- Weiß, A., Walter, F., & Scoville, N. Z. 2005, *A&A*, **438**, 533
- Wolfire, M. G., Hollenbach, D., & McKee, C. F. 2010, *ApJ*, **716**, 1191
- Yang, J., Venemans, B., Wang, F., et al. 2019, *ApJ*, **880**, 153
- Zanella, A., Daddi, E., Magdis, G., et al. 2018, *MNRAS*, **481**, 1976
- Zavala, J. A., Casey, C. M., Spilker, J., et al. 2022, *ApJ*, **933**, 242
- Zavala, J. A., Montaña, A., Hughes, D. H., et al. 2018, *NatAs*, **2**, 56
- Zhang, Z.-Y., Papadopoulos, P. P., Ivison, R. J., et al. 2016, *RSOS*, **3**, 160025